PCCP

An Experimental and Theoretical Study of the High Temperature Reactions of the Four Butyl Radical Isomers

Journal:	*Physical Chemistry Chemical Physics*
Manuscript ID	CP-ART-05-2020-002404.R1
Article Type:	Paper
Date Submitted by the Author:	19-Jul-2020
Complete List of Authors:	Randazzo, John; Argonne National Laboratory, Chemical Sciences and Engineering; North Park University, Department of Chemistry and Biochemistry Sivaramakrishnan, Raghu; Argonne National Laboratory, Chemical Sciences and Engineering Division Jasper, Ahren; Argonne National Laboratory, Chemical Sciences and Engineering Division Lynch, Patrick; University of Illinois at Chicago, Mechanical and Industrial Engineering Sikes, Travis; Argonne National Laboratory, Chemical Sciences and Engineering Tranter, Robert; Argonne National Laboratory, Chemical Sciences and Engineering

SCHOLARONE™
Manuscripts

ARTICLE

An Experimental and Theoretical Study of the High Temperature Reactions of the Four Butyl Radical Isomers

John B. Randazzo,[a,†] Raghu Sivaramakrishnan, [a] Ahren W. Jasper, [a] Travis Sikes, [a] Patrick T. Lynch [c] and Robert S. Tranter*[,a]

Received 00th January 20xx,
Accepted 00th January 20xx

DOI: 10.1039/x0xx00000x

The high temperature gas phase chemistry of the four butyl radical isomers (*n*-butyl, *sec*-butyl, *iso*-butyl, and *tert*-butyl) was investigated in a combined experimental and theoretical study. Organic nitrites were used as convenient and clean sources of each of the butyl radical isomers. Rate coefficients for dissociation of each nitrite were obtained experimentally and are at, or close to, the high pressure limit. Low pressure experiments were performed in a diaphragmless shock tube with laser schlieren densitometry at post-shock pressures of 65, 130, and 260 Torr and post-shock temperatures of 700 - 1000 K. Additional experiments were conducted with *iso*-butyl radicals at 805 K and 8.7 bar to elucidate changes in mechanism at higher pressures. These experiments were performed in a miniature shock tube with synchrotron-based photoionization mass spectrometry. The mass spectra confirmed that scission of O-NO bond is the primary channel by which the precursors dissociate, but they also provided evidence of a minor channel (< 0.4 %) through HNO loss and formation of an aldehyde. These high pressure experiments were also used to determine the disproportionation/recombination ratio for iso-butyl radicals as 0.3. Reanalysis of the lower-temperature literature and the present data yielded rate constants for the disporportionation reaction, iso-butyl + iso-butyl = iso-butene + iso-butane. A chemical kinetics model was developed for the reactions of the butyl isomers that included new paths for highly energized adducts. These adducts are formed by the addition of H, CH_3 or C_2H_5 to the butyl radicals. Accompanying theoretical investigations show that chemically activated pathways are competitive with stabilization of the adduct by collision at the conditions of the laser schlieren experiments. These calculations also show that at 10 bar and T < 1000 K stabilization is the only important reaction, but at higher temperatures, even at 10 bar, chemically activated product channels should also be considered. Branching fractions and rate coefficients are presented for these reactions. This study also highlights the importance of the radical structure for determining branching ratios for disproportionation and recombination of alkyl radicals, and these were facilitated by theoretical calculations of recombination rate coefficients for the four butyl radical isomers. The results reveal previously unknown features of butyl radical chemistry at conditions that are relevant to a wide range of applications and reaction mechanisms are presented that incorporate pressure dependent rate coefficients for the key steps.

Introduction

The gas phase chemistry of alkyl radicals underpins areas of fundamental and practical importance. For example, at atmospheric temperatures the radicals are stable and participate in a wide variety of addition reactions. At the other extreme of temperature, e.g. $T > 1100$ K alkyl radicals dissociate rapidly and essentially are sources of reactive species including hydrogen atoms and methyl radicals. However, in the auto-ignition region (roughly 500 - 900 K) the chemistry of the radicals is complex and in the absence of molecular oxygen there is a rich competition between decomposition, recombination and disproportionation, and reactions with other radicals/molecules. Elementary studies of radicals at pressures of more than a few Torr are quite rare in this temperature region, even for simple alkyl radicals. In shock tube studies this is in part due to the difficulty of thermally generating radicals under these conditions on timescales compatible with the experiments. In prior work, we have studied reactions of an unsaturated radical[1] and, C_2/C_3 alkyl radicals[2] in the 700 – 1000 K range in the well-defined reaction environment behind incident shock waves. In these studies, alkyl and alkenyl nitrites proved to be clean, suitable radical precursors. At the lower temperatures of this range, the recombination and disproportionation reactions were the most important sinks of the radicals. As the temperature was increased, ethyl and *iso*-propyl radicals dissociated by ejecting an H-atom, whereas *n*-propyl eliminated a CH_3 radical. Rates of dissociation of ethyl and *iso*-propyl were slow over the entire

[a] *Chemical Sciences and Engineering Division, Argonne National Laboratory, 9700 S. Cass Avenue, Lemont, IL 60439, USA.*
[b,2] *Department of Mechanical and Industrial Engineering, University of Illinois at Chicago, 842 W. Taylor St., Chicago IL 60607, USA.*
* *Corresponding author: tranter@anl.gov*
† *Present address: Department of Chemistry and Biochemistry, North Park University, 3225 West Foster Ave, Chicago, IL 60625, USA*
Electronic Supplementary Information (ESI) available: Tables of experimental conditions; reaction mechanisms. See DOI: 10.1039/x0xx00000x

experimental range whereas secondary reactions of CH_3 and *n*-propyl had to be accounted for at T > 850 K.

In this work, we extend the study of alkyl radicals in the 700 - 1000 K range to the C_4 radicals: *n*-butyl; *sec*-butyl; *iso*-butyl; *tert*-butyl. These radicals were generated from C_5 nitrite isomers which are shown in Table 1. This group of isomers cover primary, secondary and tertiary sites as well as increasing degrees of substitution and, hence, provides a test for the role of steric hindrance. Furthermore, the C_4 alkyl radicals were expected to

Table 1:Structures and names off the pentyl nitrites and the butyl radicals produced by their pyrolysis

Pentyl nitrite and synonyms	Structure	Radical name and synonym	Radical structure
iso-pentyl nitrite 3-methylbutyl nitrite $(CH_3)_2CHCH_2CH_2ONO$		*iso*-butyl *i*-C_4H_9	
2-methylbutyl nitrite $CH_3CH_2CH(CH_3)CH_2ONO$		*sec*-butyl *s*-C_4H_9	
neo-pentyl nitrite 2,2-dimethylpropyl nitrite $(CH_3)_3CCH_2ONO$		*tert*-butyl *t*-C_4H_9	
n-pentyl nitrite $CH_3(CH_2)_4ONO$		*n*-butyl *n*-C_4H_9	

be more labile than the C_2 and C_3 radicals and thus the decomposition reactions were anticipated to play a larger role. The four species were studied in the same diaphragmless shock tube apparatus with laser schlieren densitometry (DFST/LS) as the earlier studies. The DFST/LS experiments were conducted at relatively low reaction pressures, 65 to 250 Torr. To explore changes in chemistry at high pressure, ~9 bar, additional experiments with *iso*-pentyl nitrite were conducted in a miniature shock tube equipped for time-resolved, photoionization mass spectrometry (PIMS). The two datasets are complementary and allow for a more complete understanding of the reaction mechanism. As noted by Randazzo et al.,[2] the secondary chemistry of alkyl radicals can be quite complex due to competition between several reactions that are all strongly exothermic and influence the DFST/LS results. The PIMS data provided some guidance for constraining the reaction mechanisms. A complementary theoretical chemistry study was also performed that provided essential constraints on rate coefficients and branching ratios for developing accurate simulations and gaining further insight into the mechanisms. The theoretical study also allowed the results to be extrapolated to a wide range of conditions for broader usage.

An important set of reactions that came to light during the theoretical study are so-called “well-skipping” reactions, which are sometimes called “formally direct” reactions.[3–5] Well-skipping reactions are elementary reactions that proceed via multiple transition states, each associated with some more direct chemical process, and thus, phenomenologically, well-skipping reactions appear to “skip” the formation of conventionally assumed intermediates.[3] The importance of well-skipping reactions has been discussed in other contexts, such as low-temperature oxidation,[4,5] and in high-temperature flames.[6] Here we show that these processes are associated with energized adducts (chemically activated alkanes) created by addition of H, CH_3, and C_2H_5 radicals to C_4 alkyl radicals in the range of the present LS studies. Specifically, in the conventional picture, the initial adducts are assumed to be stabilized and subsequently decompose via a separate elementary reaction, with each process described by separate thermal rate coefficients. Well-skipping reactions, on the other hand, phenomenologically connect the bimolecular reactants directly to bimolecular product channels and are associated with reaction rate coefficients distinct from either of the conventional ones for stabilization and decomposition. The experimental and theoretical work are combined to produce kinetic mechanisms for each of the four systems and the similarities and differences are discussed.

Table 2: DFST/LS experimental conditions.

Nitrite	# of shocks	% in Kr	T_2 / K	P_2 /Torr
iso-pentyl	45	1.0, 2.0	716 - 967	65, 130, 250
2-methylbutyl	41	0.5, 1.0, 2.0	698 – 96	65, 130, 250
neo-pentyl	30	1.0, 2.0	714 – 955	130, 250
n-pentyl	25	1.0, 2.0	713 – 1006	65, 130, 250

Methods

Diaphragmless shock tube/Laser schlieren densitometry

Low pressure experiments were performed in a diaphragmless shock tube (DFST)[7,8] equipped with laser schlieren densitometry.[9,10] The DFST is actuated by operating a fast-acting valve which separates the driver and driven sections and replaces the more traditional diaphragm. This technique creates reproducible shock waves with well-controlled, predictable

This journal is © The Royal Society of Chemistry 20xx

Please do not adjust margins

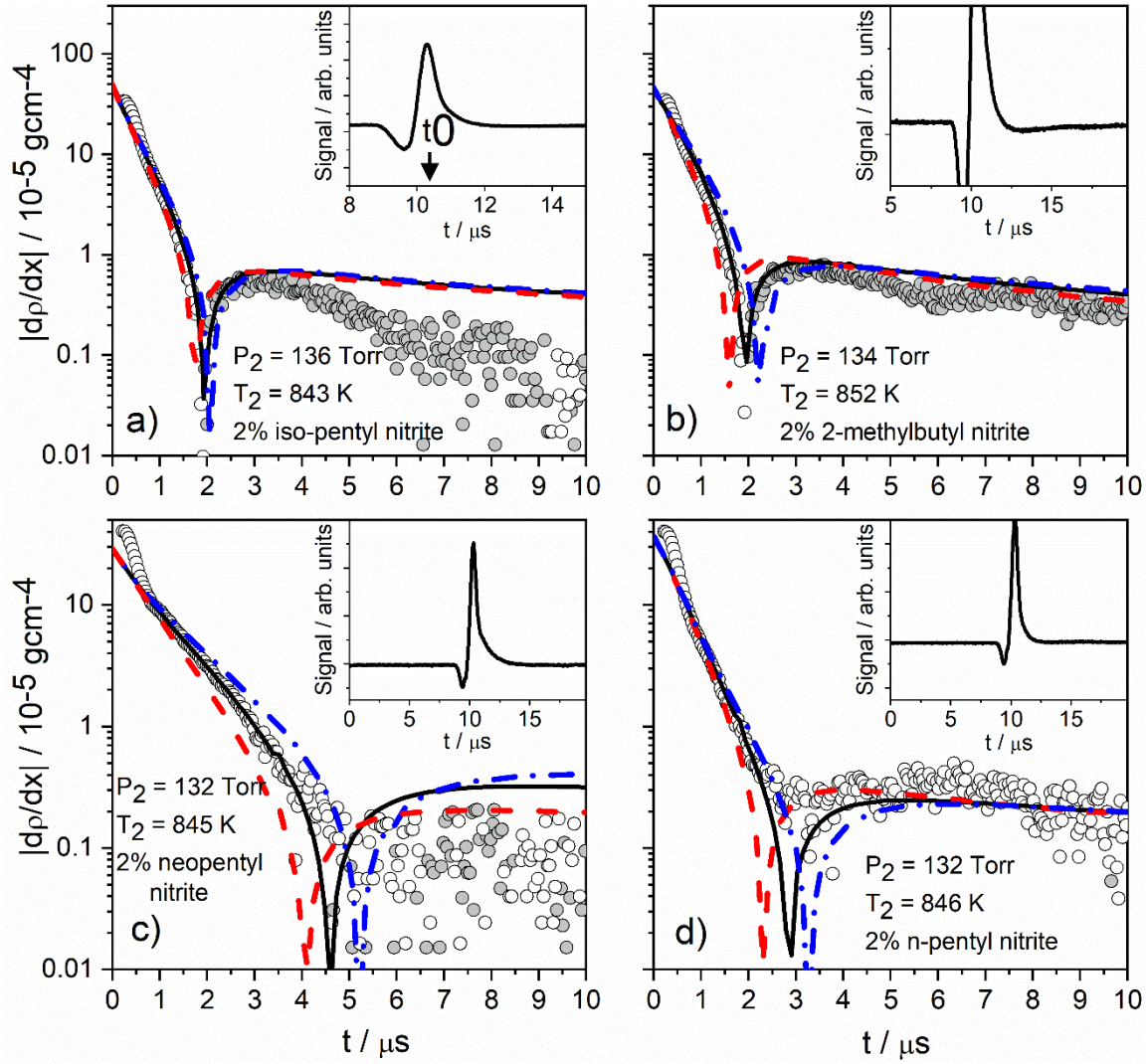

; Figure 1: Semi-log plots of absolute density gradients, best-fit simulations and the corresponding raw LS signals (insets). An example is shown for each of the four nitrites at similar reaction conditions. The location of t_0, the start of chemical reaction, is indicated in the inset of panel (a). In the main panels, the experimental data are represented by points and simulations by lines. Open circles are positive dρ/dx and shaded circles are negative dρ/dx. Solid line – best fit. Red dash line and blue dash dot lines show the sensitivity to variation of a rate coefficient to an increase of decrease of a factor of 2, respectively: a) $k_{1.6}$; b) $k_{2.7}$; c) $k_{3.5}$; d) $k_{4.6}$.

conditions in the shock wave. The temperatures, T_2 (700 – 1000 K), and pressures, P_2 (65 – 250 Torr), behind the incident shock were calculated from measured shock velocities and initial conditions assuming frozen shock conditions. The reaction conditions for each nitrite are summarized in Table 2. The shock velocities were obtained from the time taken for the incident shock wave to pass between pressure transducers centered on the observation point. The uncertainty in velocity was estimated as 0.2% (which results in an uncertainty of 4 – 6 K in T_2).

Laser schlieren densitometry measurements were taken behind incident shock waves by measuring the deflection of a narrow laser beam, which was directed across the shock tube perpendicular to the direction of propagation of the shock wave, with a split photodiode.[9,10] The laser beam was deflected by density gradients that are initially dominated by the incident shock wave and then by axial density gradients (dρ/dx) in the shock-heated gases resulting from chemical reactions. The time dependent angular deflection, ϑ, is given by Eqn. 1.[9,10]

$$\theta = \frac{3}{2} K_L W \frac{d\rho}{dx} \qquad (1)$$

where K_L is the molar refractivity of the mixture, and W is the shock tube width (6.35 cm). The molar refractivity of Kr (6.367 cm^3 mol^{-1}) was taken from Gardiner.[11] The molar refractivities of 2-methylbutyl nitrite (30.5 cm^3 mol^{-1}), *n*-pentyl nitrite (30.7 cm^3 mol^{-1}), and *neo*-pentyl nitrite (30.9 cm^3 mol^{-1}) were obtained from Chemspider.[12–14] The Lorentz-Lorenz equation[11] was used to calculate the molar refractivity of *iso*-pentyl nitrite (31.556 cm^3 mol^{-1}) from the density, ρ, and refractive index, η, (Sigma Aldrich: ρ = 0.872 g/cm^3 at 25 °C, η = 1.386). It was assumed that the molar refractivity does not change over the observation time, which is a good approximation for dilute mixtures in this study.

The density gradient due to chemical reaction is described by:[9,10]

$$\frac{d\rho}{dx} \propto \sum_j r_j (\Delta H_j - C_p T \Delta N_j) \qquad (2)$$

Please do not adjust margins

where r is the rate of reaction, ΔH is the enthalpy of reaction, C_p is the mixture heat capacity, T is the temperature, and ΔN is the change in mole number, summed over all reactions, j. In general, the term $r_j \Delta H_j$ dominates the expression, and thus the density gradient is most sensitive to reactions that have a high rate of reaction and/or high absolute enthalpy of reaction. The $C_p T \Delta N_j$ term typically evaluates to 10 - 15 kcal/mol rendering the LS measurements insensitive to mildly endothermic reactions. However, these reactions are included in simulations to accurately describe the chemistry. Typical examples of the raw signals and corresponding density gradients, at similar reaction conditions, for the four nitrites are shown in Fig. 1.

The time-dependent density gradients from the LS experiments were simulated, Fig. 1, in an iterative manner using a chemical kinetics code for reaction behind shock waves based on the methodology of Gardiner et al.[15] The chemical kinetic mechanisms are based on the generic mechanism for pyrolysis of alkyl nitrites in Ref. [2] with appropriate modifications for each of the nitrites. Key features of the mechanisms are shown in Tables 3 (*iso*-pentyl and 2-methylbutyl nitrites) and 4 (*neo*-pentyl and *n*-pentyl nitrites) with the full mechanisms given in the Supplementary Material. From here on reaction numbers refer to Tables 3 and 4. All reactions were treated as reversible, and reverse rate coefficients were determined from equilibrium constants and detailed balance. Rate coefficients were taken from a variety of sources including 1) previous DFST/LS experiments under similar conditions, 2) literature data, using pressure-dependent expressions when available, and 3) theoretical calculations. In the initial rounds the secondary chemistry was optimized and in the final round of simulations, only the rate of dissociation of the alkyl nitrite was varied to obtain the best fit to each experiment.

Thermodynamic data for most species were taken from Goos et al.,[16] with a few exceptions. Thermodynamic properties for each of the nitrite species were calculated via group additivity estimates by Reaction Mechanism Generator [17,18] and used to generate a temperature-dependent polynomial over the range of experimental conditions. For NO, H_2CO, CH_3, and C_2H_6 the data were from Active Thermochemical Tables, version 1.122.[19]

High Repetition Rate Shock Tube

High-pressure experiments were performed behind reflected shock waves in a miniature high repetition rate shock tube (ANL-HRRST).[20] The shock tube was coupled to a time-of-flight mass spectrometer (TOF-MS) by a differentially pumped molecular beam sampling (MBS) interface.[20,21] The reflected shock conditions, temperature, T_5, and pressure, P_5, were determined in a similar manner to shock conditions in the DFST with similar uncertainty in the accuracy of the incident shock velocity. The ANL-HRRST has a driven section bore of 6.35 mm and an overall length of ~650 mm. The driver section is a fast-acting, high-pressure solenoid valve.[20] Operation of the ANL-HRRST is fully automated, and it is normally fired at a rate of 1 Hz (i.e. one experiment every second). The reaction conditions are very reproducible. For example, considering 1000 shocks from the current work T_5 = 806 K with σ_{SD} = 7 K and P_5 = 8.6 bar with σ_{SD} = 0.13 bar, where σ_{SD} is the standard deviation. Consequently, a large number of experiments can be rapidly acquired and signal averaged to obtain sufficient signal/noise (S/N). For every experiment, a large number of parameters from the shock tube are recorded along with time dependent mass spectra. These data allow experiments to be binned in narrow ranges of T_5 and outliers to be rejected in post-processing. After outliers were removed (about 2% of the experiments) the remaining experiments fell in a sufficiently narrow range that further binning by T_5 was unnecessary. The majority of outliers were caused by a pressure transducer misfiring, which created an anomalous time interval resulting in an erroneous incident shock velocity. When the anomalous time interval was excluded from the calculation of T_5 and P_5 then the conditions were consistent with the rest of the dataset. Thus, although the outliers were excluded from determining the average shock conditions the mass spectra were included in the ensemble average.

This journal is © The Royal Society of Chemistry 20xx

Please do not adjust margins

ARTICLE

Table 3: Abridged mechanisms for the pyrolysis of *iso*-pentyl nitrite and 2-methylbutyl nitrite.

#	Reaction	log A	n	E_a/R	log k $_{800\ K}$	$\Delta H_{r,\ 298\ K}$	Ref.
1.1	*iso*-pentyl nitrite = *i*-$C_5H_{11}O$ + NO[j]	46.413	-9.565	25586	4.76	40.7	P.W.[a]
1.2	*i*-$C_5H_{11}O$ = *i*-C_4H_9[j] + H_2CO[j]	22.728	-2.80	7669	10.44	11.9	[22b]
1.3	*i*-C_4H_9 = CH_3 + C_3H_6[j]	34.994	-6.95	17976	5.06	22.1	[23a,c]
1.4	*i*-C_4H_9 + *i*-C_4H_9 = 2,5-DMH	15.552	-1.032	-178	12.65	-88.1	P.W.[d]
1.5	*i*-C_4H_9 + *i*-C_4H_9 = *i*-C_4H_8 [j]+ *i*-C_4H_{10}[j]	2.336	3.1	-1390	12.09	-71.7	[24e]
1.6	*i*-C_4H_9 + CH_3 = *i*-C_5H_{12}[j]	69.958	-17.50	11575	13.02	-89.4	P.W.[a]
1.7	*i*-C_4H_9 + CH_3 = C_2H_5 + *i*-C_3H_7	67.235	-15.50	18200	12.33	-2.45	P.W[a]
1.8	*i*-C_4H_9 + CH_3 = s-C_4H_9 + CH_3	47.600	-9.79	27.744	11.61	-1.15	P.W.[a]
2.1	2-methylbutyl nitrite = $CH_3CH_2CH(CH_3)CH_2O$ + NO	117.60	-31.21	41116	4.67	40.7	P.W.[a]
2.2	$CH_3CH_2CH(CH_3)CH_2O$ = *s*-C_4H_9 + H_2CO	22.728	-2.80	7669	10.44	16.5	[22f]
2.3	*s*-C_4H_9 = C_3H_6 + CH_3	61.526	-15.0	24840	4.63	17.5	[25a,g]
2.4	*s*-C_4H_9 + *s*-C_4H_9 = 3,4-DMH	13.966	-0.84	-660	11.90	-95.8	P.W.
2.5	*s*-C_4H_9 + *s*-C_4H_9 = 1-C_4H_8 + *n*-C_4H_{10}	13.584	-0.84	-660	11.42	-69.6	[24h]
2.6	*s*-C_4H_9 + *s*-C_4H_9 = 2-C_4H_8 + *n*-C_4H_{10}	13.584	-0.84	-660	11.42	-72.4	[24h]
2.7	CH_3 + *s*-C_4H_9 = *i*-C_5H_{12}	69.666	-17.3	12039	13.05	-94.0	P.W.[a]
2.8	CH_3 + *s*-C_4H_9 = *i*-C_3H_7 + C_2H_5	70.700	16.5	19550	12.19	-7.09	P.W.[a,i]

$k = AT^n \exp(-Ea/RT)$. Units are mol, cm^3, K, and kcal.

[a] Value for 130 Torr shown

[b] by analogy with *i*-C_4H_9O.

[c] Cited value was increased by a factor of 4 to obtain the best fit to the experimental data

[d] Val Capture rate based on present VRC-TST calculations (300-2000K)

[e] Fit to data (298-800 K) from Gibian and Corley review[24] and present work

[f] by analogy with *i*-C_4H_9O

[g] Cited value was increased by a factor of 4 to obtain the best fit to the experimental data

[h] $k_{2.5} = k_{2.6} = 0.33 \times k_{2.4}$

i $k_{2.8} = 0.05 \times k_{2.7}$

[j]Species detected in HRRST/TOF-MS experiments

Table 4: Abridged mechanisms for the pyrolysis of *neo*-pentyl nitrite and *n*-pentyl nitrite.

#	Reaction	log A	n	E_a/R	log $k_{800\ K}$	$\Delta H_{r,\ 298\ K}$	Ref.
3.1	*neo*-pentyl nitrite = $(CH_3)_3CCH_2O$ + NO	12.736	-0.005	14910	4.63	40.8	P.W.[a]
3.2	$(CH_3)_3CCH_2O$ = *t*-C_4H_9 + H_2CO	22.728	-2.800	7669	10.44	11.1	[22b]
3.3	*t*-C_4H_9 = *i*-C_4H_8 + H	14.244	-0.010	19218	3.80	34.8	[26]
3.4	*t*-C_4H_9 + *t*-C_4H_9 = 2233-TMB	14.136	-0.920	-350	11.66	-81.7	[27]
3.5	*t*-C_4H_9 + *t*-C_4H_9 = *i*-C_4H_8 + *i*-C_4H_{10}	14.627	-0.920	-350	12.15	-62.8	[24c]
3.6	*t*-C_4H_9 + H = *i*-C_4H_{10}	72.186	-17.670	13489	13.57	-97.5	P.W.[a]
3.7	*t*-C_4H_9 + H = *i*-C_4H_8 + H_2	72.487	-17.670	13489	13.87	-69.4	Est.[a,d]
3.8	*t*-C_4H_9 + H = *i*-C_3H_7 + CH_3	36.304	-6.230	10393	12.58	-8.72	P.W.[a]
4.1	*n*-$C_5H_{11}ONO$ = *n*-$C_5H_{11}O$ + NO	22.419	-2.830	17699	4.60	40.8	P.W.[a]
4.2	*n*-$C_5H_{11}O$ = *n*-C_4H_9 + H_2CO	21.196	-2.440	8474	9.51	12.4	[22e]
4.3	*n*-C_4H_9 = C_2H_4 + C_2H_5	31.500	-6.080	16391	4.95	21.6	[23a,f]
4.4	*n*-C_4H_9 + *n*-C_4H_9 = C_8H_{18}	15.696	-1.000	-40	12.81	-89.0	P.W.[a]
4.5	*n*-C_4H_9 + *n*-C_4H_9 = 1-C_4H_8 + *n*-C_4H_{10}	14.842	-1.000	-40	11.96	-64.2	[24g]
4.6	C_2H_5 + *n*-C_4H_9 = *n*-C_6H_{14}	69.390	-17.00	12700	13.17	-88.1	P.W.[a]
4.7	C_2H_5 + *n*-C_4H_9 = C_2H_6 + 1-C_4H_8	68.293	-17.00	12700	12.07	-63.2	[24h]
4.8	C_2H_5 + *n*-C_4H_9 = C_2H_4 + *n*-C_4H_{10}	68.168	-17.00	12700	11.95	-65.7	[24i]

$k = AT^n \exp(-Ea/RT)$. Units are mol, cm^3, K, and kcal.

[a] Value for 130 Torr shown

[b] by analogy with *i*-C_4H_9O

[c] $k_{3.5} = 3.1 \times k_{3.4}$

[d] $k_{3.7} = 2 \times k_{3.6}$

[e] by analogy with *n*-C_4H_9O

[f] Cited value was decreased by a factor of 2 to obtain the best fit to the experimental data, making it similar to the value recommended by Zheng and Blowers[28]

[g] $k_{4.5} = 0.14 \times k_{4.4}$

[h] $k_{4.7} = 0.08 \times k_{4.6}$

[f]i$k_{4.8} = 0.06 \times k_{4.6}$

The driven section of the ANL-HRRST was terminated by a nozzle (0.75 mm tall, 0.20 mm orifice, and 110 degree included angle) which formed the first stage of the MBS. Gases eluted continuously from the shock tube through the nozzle and formed a supersonic jet, thereby quenching reaction and preserving the composition as the gases left the shock tube.[7] A skimmer (Beam Dynamics, Model 2, 0.2 mm orifice) sampled gases from the centerline of the jet, formed them into a molecular beam, and directed them into the ion source of the TOF-MS. The skimmer was located approximately 10 nozzle diameters (2.0 mm) downstream of the nozzle, and the skimmer exit was 28 mm from the center of the ion source. These small separations between the components of the MBS setup help minimize the mass discrimination effects described by Cool et al.[29] The setup is similar to that described in Ref.[21] and MBS between a shock tube and a TOF-MS is described in Ref. [7]

Photoionization Mass Spectrometry

The TOF-MS (Kasedorf CF5B) was operated in reflectron mode. Mass spectra were acquired by digitizing the analog signal from its multi-channel plate detector. Digitization was performed using a PCIe DAQ card (GAGE-Applied, Compuscope EON) at 1 GS/s with 12-bit vertical resolution. The board was triggered at 100 kHz via a delay generator (SRI DG645) and data were acquired for 8 µs allowing ions up to m/z 230 to be detected. An identical pulse, 1 µs duration, from a second channel triggered extraction of ions from the TOF-MS ion source for analysis. For each shock, data were acquired for 3 ms giving 300 discrete mass spectra. The data acquisition period was timed to obtain data from the pre-shock region (unreacted gases), through reaction in the reflected shock wave to after quenching by rarefaction waves in the ANL-HRRST.

Many of the reagents and products in this study would fragment extensively in the TOF-MS if electron ionization (EI) were used, making identification of species difficult. Consequently, photoionization (PI), a "softer" ionization technique which typically reduces fragmentation, was used instead of EI. Photons were obtained from synchrotron radiation at the Advanced Light Source (ALS) Chemical Dynamics Beamline 9.0.2, T2 end station, at Lawrence Berkeley National Laboratory. The photon energy was tunable over a broad range (7 - 24 eV). The T2 end station is not equipped with a monochromator, so

This journal is © The Royal Society of Chemistry 20xx

Please do not adjust margins

the photon energy is set by the undulator gap, resulting in a bandwidth of ~0.3 eV. This limits resolution of ionization thresholds and identification of species by photoionization spectra, although the resolution is generally adequate for this work. The undulator not only generates light at the desired energy but also at higher harmonic energies. This unwanted high-energy light was mostly removed by an argon gas filter that transmitted photons with energies below 15.7 eV. However, a small amount of high-energy photons passed through the gas filter causing fragmentation in the ion source of the TOF-MS and the appearance of species that had ionization energies greater than the fundamental photon energy from the undulator. To account for the effects of high-energy harmonic light, experiments were repeated with a 1 mm thick slab of MgF_2 that transmitted photons below 11.2 eV. The MgF_2 filter was mounted on a linear translation stage and could be inserted into or withdrawn from the beam path. The slab was positioned between the end of the ultra-high vacuum beamline and high-vacuum mass spectrometer chamber, about 150 mm from the center of the TOF-MS ion source. In this position the MgF_2 filter was easily viewed and repositioned as needed, about every 30 minutes due to burning from the intense VUV beam. The VUV beam is < 600 μm in width and moving the filter 1 - 2 mm was sufficient. The filter attenuates the photon beam by about 50% at 10.5 eV, but this loss did not present any challenges to obtaining adequate signal strengths. In practical terms, the maximum signal (a combination of photon flux and photoabsorption cross-section for a fixed concentration of a species) was observed between 10.5 to 10.8 eV. For photon energies above 10.8 eV, the signal intensity rapidly dropped until the cut-off at 11.2 eV.

The resulting spectra from all the ionization energies are assembled into a three-dimensional (3D) matrix that contains the mass to charge ratio (m/z), reaction time (t) and photon energy (PE) dependencies of the spectra. The values in the cells of the 3D matrix are the measured signal (MCP output). The datasets are similar to those described by Osborn et al.[30] from photolytic experiments in a low-pressure flow tube with photoionization mass spectrometric detection. As noted by Osborn et al. visualizing the 3D dataset is challenging, and instead, slices through the data are taken to make two dimensional (2D) projections that are represented as 2D image plots. Two projections representing t against m/z (TM) and, PE against m/z (EM) are used throughout the remainder of the discussion. Typically, 2D-plots of the TM and EM datasets are dominated by a few major features, and more revealing are vertical and horizontal slices through the TM and EM projections. Vertical slices from a TM dataset reveal the reaction time dependence of a species, while those from an EM dataset give the PE dependence and hence photoionization spectrum. Horizontal slices from either the TM or EM sets yield traditional mass spectra (signal strength vs. m/z) over a range of PE or t, respectively. By selecting different segments of the 3D matrix to build the TM and EM datasets various aspects of the experimental data can be focused on.

Reagents and mixtures

Iso-pentyl nitrite was purchased from Sigma Aldrich (96%). 2-methylbutyl, *neo*-pentyl, and *n*-pentyl nitrites were synthesized from 2-methyl butyl alcohol, *neo*-pentyl alcohol and *n*-pentyl alcohol respectively, by the procedure used in Tranter et al.[1] and Randazzo et al.[2]

For the DFST/LS experiments, reagent mixtures of 0.5 – 2.0% nitrite dilute in krypton were prepared manometrically in a 50 L glass vessel. Liquid reagents were degassed with liquid nitrogen prior to use. The bath gas, krypton (Airgas, 99.999%) was used as supplied. The mixtures were stirred for at least one hour with a PTFE-coated magnetic stirrer prior to use.

Mixture preparation for the ANL-HRRST/TOF-MS experiments is more complicated as the rate of consumption of the reagent mixture precludes preparation of a single tank by traditional methods. Instead, the reagent mixtures are prepared on demand by a purpose-built flow mixing system and stored in a 4.7 L stainless steel tank. Operation of the apparatus is fully automated and controlled through a software interface written in LabVIEW. As the mixture in the tank is consumed, fresh mixture is added to the tank on demand. *iso*-Pentyl nitrite was placed in a stainless steel high-pressure bubbler (500 psig maximum working pressure). Air was evacuated from the bubbler, and it was then purged with argon, the bath gas. To prepare a mixture, argon (50 psia) was bubbled through the liquid at 23 °C, entraining vapour. The argon/nitrite mixture was admitted to a small mixing chamber[20] via a mass flow controller and blended with additional argon metered by a second mass flow controller to produce the desired concentration of *iso*-pentyl nitrite dilute in argon. The estimated vapour pressure of *iso*-pentyl nitrite is 44 Torr at 25 °C[31] and was measured as 40 Torr at 22 °C in the lab. The mixture in the storage tank had a concentration of *iso*-pentyl nitrite of 0.26 ± 0.02% accounting for uncertainty in the vapour pressure.

Synthesis of pentyl nitrites: Each nitrite was prepared by first making a mixture of the corresponding alcohol (i.e., 2-methylbutyl, *neo*-pentyl, or *n*-pentyl alcohol; 37 mmol) and excess $NaNO_2$ (74 mmol). To this mixture, 20 mL of 9.25% HCl (aqueous) was added dropwise over the course of 10 minutes. During addition of the acid, the solution refluxed gently, and after a few minutes, brown gas formed in the headspace above the solution, indicating the formation of NO_2 gas as a side product. After addition of HCl was completed, the solution continued to mix for an additional 15 minutes before stirring was ceased. The solution was then removed from the ice bath and allowed to separate into two distinct layers. The organic layer was collected and washed twice with a saturated NaCl solution and then dried over Na_2SO_4, resulting in a clear yellow liquid.

Theory

High-pressure limit (capture) rate coefficients for *iso*-C_4H_9+*iso*-C_4H_9, *iso*-C_4H_9 + CH_3, *sec*-C_4H_9 + *sec*-C_4H_9, *sec*-C_4H_9 + CH_3, *n*-C_3H_7 + *n*-C_3H_7, *iso*-C_3H_7 + CH_3, *iso*-C_3H_7 + C_2H_5, and *n*-C_4H_9 + C_2H_5 were

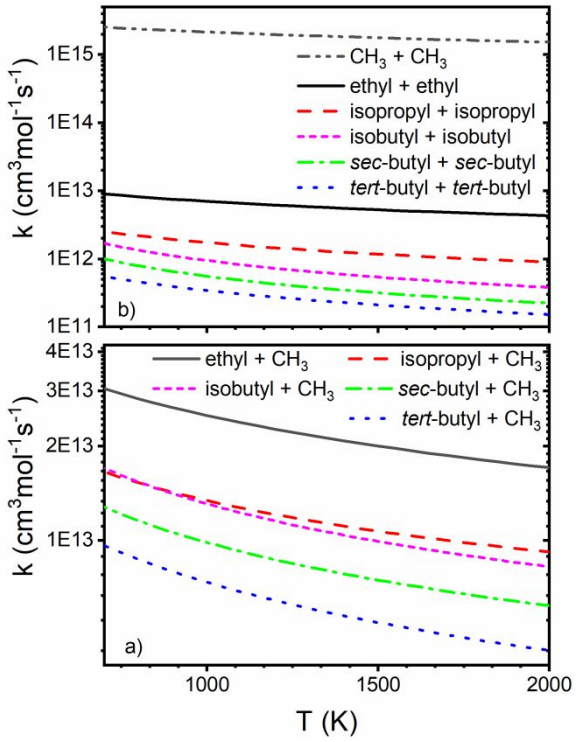

Figure 2:: a) R+CH3 and b) R+R combination rate coefficients. R=CH3, ethyl, *iso*-propyl, and *tert*-butyl were studied by Klippenstein et al.[27] R=*iso*-butyl and sec-butyl were calculated in the present work through master equation calculations.

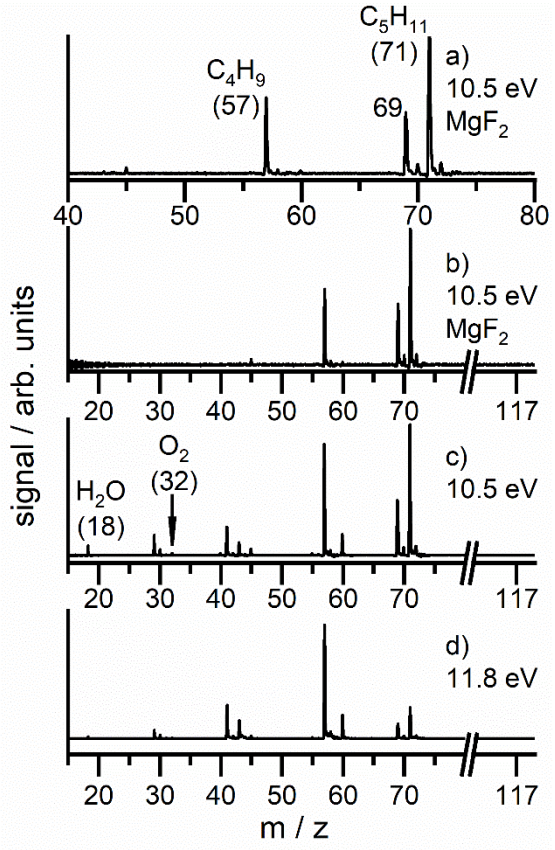

Figure 3:: Mass spectra of 0.25% *i*-pentyl nitrite dilute in Ar. Labels indicate assignments and nominal masses. Panels a and b: 10.5 eV with MgF_2 filter to remove high harmonic light. Panel a shows an expanded portion of panel b. Panel c: 10.5 eV but without the MgF_2 filter. Note the appearance of m/z 18 and 32 that are absent in b; Panel d: 11.8 eV and no MgF_2 filter.

calculated using variable reaction coordinate transition state theory[32,33] (VRC-TST), CAS(2e,2o)PT2/cc-pVDZ energies, and a one-dimensional basis set and correlation energy correction. We used the same theoretical strategy that was previously used to compute capture rates for several alkyl radical – alkyl radical reactions and where quantitative agreement with experimental results was demonstrated for C_2H_5 + CH_3 and the self-reactions of CH_3, C_2H_5, *iso*-C_3H_7, and *tert*-C_4H_9.[27]

Under experimental conditions where there is significant dissociation of the butyl radicals, care was taken to account for potential secondary reactions that may influence the reactions characterized here. Of particular concern are the reactions of butyl radicals with their dominant β-scission radical products (H, CH_3, and C_2H_5). While recombination is expected to be the dominant channel for such radical-radical reactions at T < 1000 K, the lower pressures in the DFTS/LS experiments may potentially lead to radical-radical well-skipping (or "formally direct") product channels opening up, i.e., H + *tert*-C_4H_9 = CH_3 + C_3H_6. Consequently, the rovibrational properties of such radical-radical reactants, adducts, and radical-radical product channels were determined at the M06-2X/cc-pvtz level of theory. Higher level energy estimates for these stationary points were obtained using the CCSD(T)/cc-pV∞Z method with the infinite basis set limits estimated from an extrapolation of results obtained from sequences of cc-pVnZ where n = (T,Q) basis sets.[34,35] Master equation calculations were performed with the VARIFLEX code[36] using the ab initio based energetics and molecular properties to obtain theoretical rate coefficients. The transition state partition functions are evaluated using Phase Space Theory (PST) for the barrierless association channels. The availability of rigorous VRC-TST predictions[27,37] for the high-pressure limit recombination rate constants for all relevant radical (H, CH_3, C_2H_5) + butyl (*tert*-, *iso*-, sec-, and *n*-) radical recombination reactions afforded tests for the predictive capability of the present PST calculations. In the present PST calculations the coefficient for the R-6 potential was adjusted to fit these higher level VRC-TST $k_{rec,\infty}$ predictions. Lennard-Jones parameters for all the species were taken from the literature.[38,39] Pressure-dependent rate coefficients were calculated over the temperature range 500 – 2000 K. An exponential down model was used for the energy transfer with temperature-dependent $\langle\Delta E\rangle_{down}$ parameters that were taken from recent predictions[39] for the C_4, C_5, and C_6 alkane recombination adducts. We emphasize that the identification of important well-skipping channels for these reactions emerges as a result of the master equation. Specifically, at the high energies associated with these C_4 – C_6 adducts, the low-energy product channels have large fluxes associated with them that compete favorably with stabilization rate constants under some conditions. The latter are pressure dependent, of course, such that the importance of the well-skipping channels decreases with increasing pressure. At high temperatures relevant to

This journal is © The Royal Society of Chemistry 20xx

Please do not adjust margins

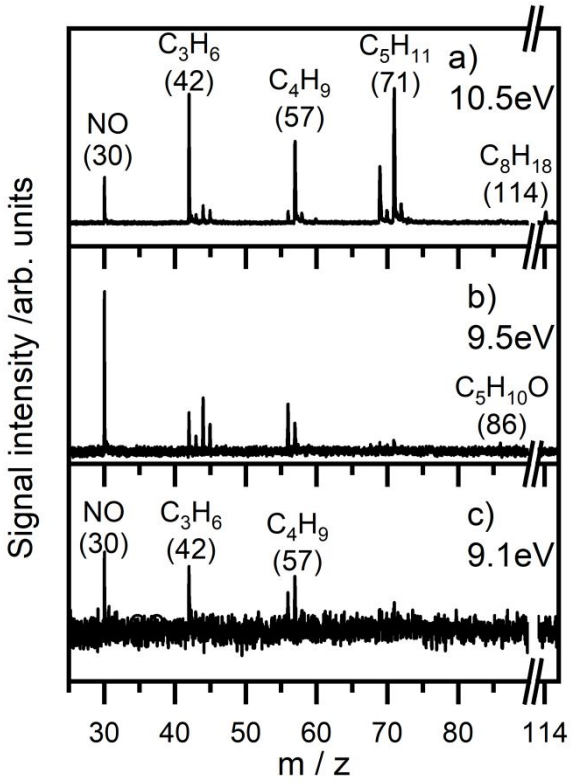

Figure 4: Mass spectra at different photon energies integrated over 0 - 130 µs following formation of the reflected shock wave. MgF2 filter inserted. 0.25% *iso*-pentyl nitrite/argon. T_5 = 807 K and P_5 = 8.7 bar.

shock tubes and flames, radical channels that are even endothermic to the initial radical-radical entrance channel can be competitive channels. Classic examples from combustion kinetics include $CH_3 + CH_3 = H + C_2H_5$,[40] and $H + C_6H_5CH_2 = CH_3 + C_6H_5$,[41] proceeding through the energized adducts (or chemically activated) ethane and toluene respectively. Notably, the relative importance of well-skipping channels and stabilization are shown here to be sensitive functions of temperature and pressure over the conditions of interest here.

Results and discussion

ANL-HRRST/TOF-MS

Two sets of experiments, with and without the MgF_2 filter in the beam path, were performed. Due to the reproducibility of the ANL-HRRST, the studies were performed at the same nominal T_5 and P_5 of 806 K and 8.7 bar respectively. Experiments with the filter were limited in energy range but showed minimal fragmentation in the ion source. In contrast, those without the filter allowed access to higher ionization energies but suffered from more fragmentation. Mass spectra without the MgF_2 window were acquired in 0.1 eV steps from 9.0 - 12.0 eV, a total of 3100 shocks. Experiments with the MgF_2 window covered 9.1 - 10.9 eV in 0.2 eV steps, 1000 shocks in total. Of the 300 mass spectra acquired per shock, 96 spectra were in the pre-shock region, before the arrival and reflection of the incident shockwave. From the remaining spectra, 30 - 60 are in a region where the reaction conditions are well characterized see for example pressure profiles in Refs. [20,42].

In Fig. 3b a horizontal slice across an EM plot at 10.5 eV is shown. The underlying data were taken from the first 80 mass spectra (0 - 800 µs from the start of data acquisition). The mass spectra are from the pre-shock region and thus show the mass spectrum of *i*-pentyl nitrite prior to shock heating. Fig. 3a shows the same dataset as Fig. 3b but for a limited range to more clearly show key species and some minor peaks. The data in Fig. 3b were taken with the MgF_2 filter inserted to remove high energy harmonic light. It is quite clear from these figures that *i*-pentyl nitrite fragments completely at 10.5 eV as no peak is observed at the parent mass, m/z 117. In fact, it was not possible to resolve m/z 117 at any PE. Strong peaks are observed at m/z 71 (C_5H_{11}), 69 (C_5H_9), and 57 (C_4H_9, *iso*-butyl radical) with minor peaks at m/z 60 and 45. The small peaks at m/z 72, 70 and 58 have the same ionization dependencies as the m/z-1 peak and the ratio of (m/z-1)/m/z is close to that expected from the natural isotopic abundance of ^{13}C accounting for noise in the data. Thus, we conclude that they are most likely the ^{13}C isotopes of the major peaks. Removing the MgF_2 filter created more fragments from *iso*-pentyl nitrite, Fig. 3c; primarily due to high harmonic energies that were previously blocked by the filter. The mass spectrum in Fig. 3c contains not only the major peaks at m/z 71, 69 and 57, but what were minor peaks at m/z 45 and 60 are now much more pronounced and additional peaks appear at m/z 29, 41, 43, 32 and 18. The only plausible identities for m/z 18 and m/z 32 are H_2O and O_2, which are present as background species in the TOF-MS chamber. The ionization energies of H_2O and O_2 are 12.62eV[43] and 12.07 eV[43] respectively, considerably higher than the 10.5 eV photons even accounting for a bandwidth of ~0.3 eV. As the photon energy is increased to 11.8 eV, Fig. 3d, the m/z 57 peak becomes dominant while the magnitude of m/z 18 remains unchanged indicating that m/z 18 is not formed by fragmentation of *iso*-pentyl nitrite.

For the remainder of the discussion only data taken from the experiments with the MgF_2 filter in place will be considered. The data set consist of 1000 shocks with T_5 = 806 K (σ_{SD} = 6.9K) and P_5 = 8.7 bar (σ_{SD} = 0.13 bar). In Fig. 4 mass spectra at different ionization energies are shown. The underlying data are integrated from the time of the reflection of the shock wave to 130 µs after shock reflection, i.e. the first 130 µs of reaction. The mass spectra contain peaks from dissociation of the parent molecule and the products of subsequent reactions. The time histories for selected species are shown in Fig. 5. In these plots the time traces are integrated over 9.1 to 10.9 eV.

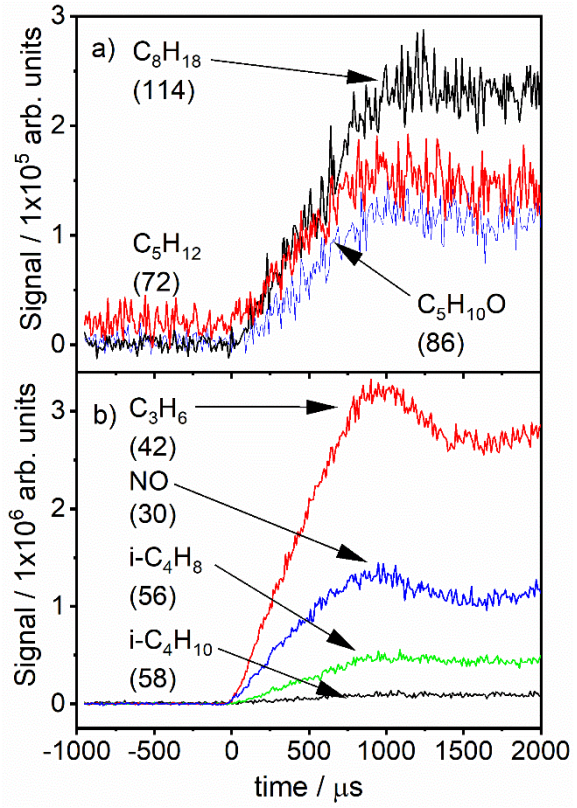

Figure 5: Time dependencies of key species from pyrolysis of 0.25% *iso*-pentyl nitrite/Ar. The spectra are integrated over 9.1 - 10.9 eV and the MgF_2 filter was inserted. 0 μs defines the start of reaction. The small m/z 72 signal prior to 0 μs is due to the 13C isotope of m/z 71 from photo fragmentation of *iso*-pentyl nitrite.

A schematic mechanism for dissociation of *iso*-pentyl nitrite and the *i*-butyl radical is given in Fig. 6. The dominant initial step yields an alkoxy radical (m/z 87) and NO (m/z 30), reaction 1.1. There is no evidence of m/z 87 in Fig. 4 which is consistent with the *iso*-pentoxy radical rapidly dissociating. Reaction 1.2 yields both *iso*-butyl (m/z 57) and formaldehyde (m/z 30). Thus, the m/z 30 peak in Fig. 4 could be due to a combination of cations from formaldehyde and NO. However, the ionization energy of formaldehyde is 10.88 eV[43] while that of NO is 9.26 eV.[43] Consequently, m/z 30 in Figs. 4a-c is due only to NO and acts as a surrogate for consumption of *iso*-pentyl nitrite. Furthermore, m/z 30 is not present in pre-shock mass spectra, Fig. 3, but only appears after reflection of the shock wave, Fig. 5b, indicating it is not created by dissociative ionization of *iso*-pentyl nitrite.

In Fig. 4b an intriguing minor peak appears at m/z 86 and PE 9.5 eV. The peak is also present at higher PE but is not observable in Fig. 4a due to its size relative to the major peaks. Based on Randazzo et al.[2] a species of this mass was not expected here, but it is consistent with either 3-methyl butanal from elimination of HNO from *iso*-pentyl nitrite, or 2,3-dimethyl butane from recombination of *iso*-propyl radicals. The time history of m/z 86 is shown in Fig. 5a. It is absent in the pre-shock region but appears immediately upon shock reflection. The apparent ionization energy for m/z 86 is approximately 9.5 eV which is similar to the literature value for 3-methyl butanal of 9.7 eV,[43] accounting for bandwidth and S/N. The ionization

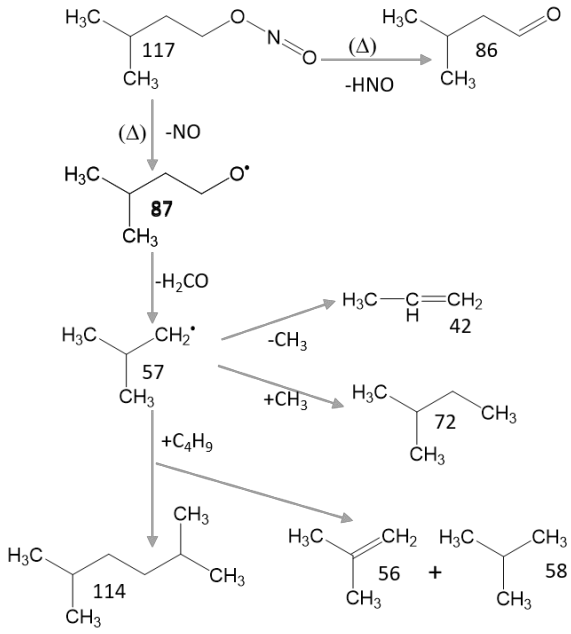

Figure 6: Thermal decomposition of *iso*-pentyl nitrite and the subsequent reactions of the *i*-butyl radical.

energy for 2,3-dimethyl butane is 10.02 eV[43] and thus too high for the m/z 86 peak at 9.5 eV. It is possible that at higher PE m/z 86 could be a combination of 3-methylbutanal and 2,3-dimethylbutane. However, 2,3-dimethylbutane would be formed by recombination of *iso*-propyl radicals which in this system are created by non-thermal reaction of CH_3 and *i*-C_4H_9 radicals, Fig. 7. For the reaction conditions of the TOF-MS experiments, 800K and ~9 bar, Fig. 7 indicates that formation of *iso*-propyl radicals is a very minor channel. Thus we conclude that m/z 86 is 3-methyl butanal and it is most likely formed by elimination of HNO from *iso*-pentyl nitrite.[1] There is a very faint signal in the mass spectra at m/z 31 and 10.5 eV that corresponds to the mass of HNO. The ionization energy of HNO is 10.1 eV.[43] The signal is barely distinguishable from noise but appears to rise at formation of the reflected shock.

Both NO and 3-methyl butanal are unique markers for two distinct paths for unimolecular dissociation of *iso*-pentyl nitrite. Consequently, if their relative concentrations can be measured then the branching ratio for the paths can be obtained. Figures 4 and 5 suggest that NO is by far the dominant species. However, the signal intensity at a particular IE is not only proportional to the concentration of a species, but also its photoionization cross-section. We define $\sigma_{x,eV}$ as the photoionization cross-section at energy, x eV. By taking ratios of the product of peak area (or height) and $\sigma_{x,eV}$ relative concentrations of species can be obtained. As indicated by Cool et al.[29] mass discrimination due to transport of species away from the centerline of the molecular beam can be significant in determining accurate concentrations. Mass discrimination factors have not been determined for the ANL-HRRST/TOF-MS, but the sampling geometry suggests they will be small. For an upper limit of the uncertainty introduced by mass discrimination factors to the estimated concentration of NO relative to 3-methyl butanal, values from Cool et al.[29] were

This journal is © The Royal Society of Chemistry 20xx

Please do not adjust margins

used. These are likely larger than in the ANL-HRRST/TOF-MS but indicate up to a factor of two uncertainty in the relative concentrations which is adequate for the current qualitative analysis. Literature photoionization cross-sections for NO are available over a broad range of energies that encompass the current work.[44–47] Photoionization cross sections for 3-methyl butanal and its daughter ions have been measured by Welz et al. from 9.5 – 11 eV.[48] For experiments with the MgF_2 filter the maximum signal strengths for m/z 30 and m/z 86, the parent ion of 3-methyl butanal, are observed at ~10.5 eV. The ratio of (m/z 86)/(m/z 30) at 10.5 eV is 0.08 and the ratio of their $\sigma_{10.5,eV}$, is 0.97. Assuming that mass discrimination is negligible an upper limit of 7.7% *iso*-pentyl nitrite pyrolyzes to 3-methyl butanal at 800 K and ~9 bar. Determining the pressure and temperature dependence of HNO elimination and the mechanism by which it occurs is beyond the scope of this study. However, the branching ratio found here is consistent with an upper limit estimated in a prior LS study.[1]

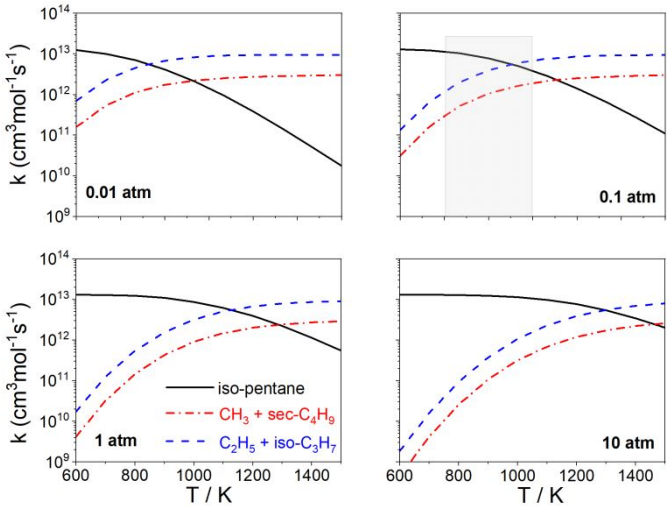

Figure 7: Rate coefficients for combination and addition-elimination reactions for *iso*-butyl+CH_3 from master equation calculations at various pressures. The shaded grey rectangle shows approximate LS experimental conditions in this study.

A reaction class that is of particular interest in this paper is the recombination and disproportionation of alkyl radicals. The recombination of two *iso*-butyl radicals gives 2,5-dimethylhexane (2,5-DMH) and the disproportionation reaction yields *iso*-butene and *iso*-butane in equal amounts. Applying a similar analysis as above to *iso*-butene (m/z 56) and *iso*-butane (m/z 58) at 10.9 eV yields a ratio of peak intensities (m/z 56)/(m/z 58) of ~3.5. The ratio of $\sigma_{10.9,eV}$ is 3.7.[49,50] While this suggests that there might be a small excess of *iso*-butane, the signal levels for m/z 86 at 10.9 eV are quite low due to attenuation by the MgF_2 filter and $\sigma_{10.9,eV}$ of *iso*-butane is quite small at 2.99 Mb.[49] Both m/z 56 and m/z 58 contain small contributions from sources other than *iso*-butene and *iso*-butane respectively. The m/z 58 peak contains a fraction equivalent to ~4.4% of the m/z 57 peak due to ^{13}C isotopes and the m/z 56 peak contains a contribution from dissociative ionization of 2,5-DMH[51] which amounts to <7% of 2,5-DMH for PE <10.5 eV. Consequently, we conclude that *iso*-butene and *iso*-butane are formed in a 1:1 ratio within experimental error.

The branching ratio between disproportionation and recombination can be estimated from the ratio of *iso*-butene and 2,5-DMH signals. The parent peak of 2,5-DMH is at m/z 114 and has an ionization threshold of about 9.76 eV,[43] which compares well with the observed value of 9.7 eV. The m/z 114 peak is small which initially suggests that 2,5-DMH may be a minor species. However, as noted above 2,5-DMH dissociatively ionizes extensively and at 10.1 eV approximately 3.7% of the fragments have m/z 56. The contribution of these fragments to the m/z 56 signal was estimated from the observed m/z 114 signal at 10.1 eV and the fragmentation pattern of 2,5-DMH at the same energy.[51] Finally, from the corrected m/z 56 signal, the m/z 114 signal at 10.1 eV and their $\sigma_{10.1eV}$,[50,52] a branching ratio of 0.3 at 800 K and 9 bar for disproportionation/recombination of *i*-butyl radicals was obtained. Gibian and Corley[24] give the disproportionation/recombination ratio as 0.079. However, this ratio is based on low temperature measurements (298 - 441K) and assumed to be valid at room temperature and essentially temperature independent. A more detailed discussion is given in the DFST/LS section. The Gibian and Corley review concludes that the disproportionation/recombination ratios obtained using 1,1'-azoisobutane as the photolysis source for *iso*-butyl radicals by Slater et al.[53] and Terry and Futrell[54] are reliable. The ratio determined by Terry and Futrell at 298K and the T-dependent (368 – 441 K) ratios determined by Slater et al. were used along with the 800K ratio from the present work and the theoretical capture rate constants from the present VRC-TST predictions to obtain rate constants for disproportionation of iso-butyl radicals. These rate constants are best fit to an Arrhenius expression represented by,

$$k_{1.5} = 2.168 \times 10^2\ T^{3.1} \exp(1390/T)\ cm^3\ mol^{-1}\ s^{-1}\ (298\text{-}800\ K) \quad (3)$$

More details on the analysis for this disproportionation reaction and an Arrhenius plot is shown in the supporting information

The next peak of note in Fig. 4 is m/z 42. The observed ionization energy is 9.5 eV, which compares reasonably well with the literature value for propene of 9.73 eV,[43] accounting for experimental artifacts. Propene is formed by ejection of a methyl group from an *iso*-butyl radical, reaction 1.3. The photoionization cross-section of propene, $\sigma_{10.5,eV}$ = 11.09 Mb,[55] is about 10% larger than that of *iso*-butene at 10.5 eV and neither species fragments at this energy. Thus a direct comparison of their peak sizes can be made to obtain relative concentrations. On this basis, the propene concentration is around a factor of 10 greater than that of *iso*-butene. These relative concentrations are similar to what would be expected based on simulations of *iso*-pentyl nitrite dissociation with the mechanism developed here.

From the calculated rate coefficients in Fig. 7d, 2-methyl butane is predicted to be the only species observed from reactions 1.6 - 1.8, addition of methyl to *iso*-butyl. Ethyl (m/z 29) is not observed at all in the mass spectra. There is a small peak at m/z 43 that could be *iso*-propyl. However, this peak has the same PE dependence as the major species at m/z 42, propene, and the size of m/z 43 is consistent with it being the ^{13}C isotope peak of

propene. The peak at m/z 72, 2-methyl butane, is very small suggesting it represents a minor species. However, the ionization energy of 2-methyl butane is 10.32 eV[43] and the photoionization spectrum is not known. Consequently, the concentration cannot be determined relative to another species.

DFST/LS

For each nitrite a broad range of experimental conditions were covered, Table 2. Example LS profiles from the different nitrites at similar T_2 and P_2 are shown in Fig. 1. For each experiment the flat region prior to arrival of the shock wave at early times in the raw signal (Fig. 1, insets) are used to establish a baseline for calculating the density gradients. The characteristic valley and peak around 10 μs in the raw profile is due to the interaction of the laser beam and shock wave as the wave passes through the beam. The start of chemical reaction, time t_0 (e.g. Fig, 1a), is obscured by the peak and is therefore located with a well-established method[9] with an accuracy of ≤ 0.2 μs. The decaying signals to the right of the large peak result from chemical reactions.

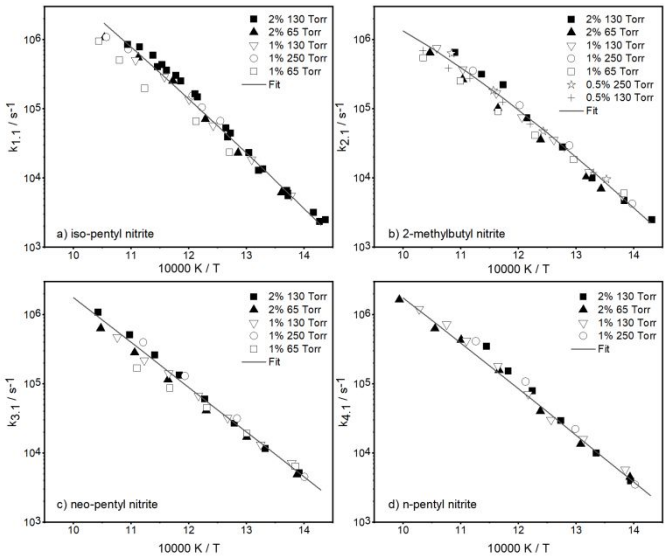

Figure 8: Arrhenius plots for the unimolecular dissociation of four $C_5H_{11}ONO$ isomers by loss of NO. RMS errors for the least squares fits (lines) are 18 to 27%.

The main panels in Fig. 1 show semi-log plots of the absolute density gradients calculated from the raw LS signal using Eqn. 1. The first several rapidly falling points are from the shock wave/laser beam interaction, which obscures the chemical signal for ~1 μs. The remaining signal can be interpreted by considering the reactions of the parent nitrites and their pyrolysis products. At early times, the density gradient is positive, indicating the prominence of endothermic reactions, particularly the dissociation of the parent nitrite and the resulting alkoxy radical. As reaction progresses, the density gradients become increasingly negative because the parent nitrite is consumed and exothermic secondary reactions, particularly radical combination and disproportionation, become dominant. The *iso*-pentyl nitrite (Fig. 1a) and 2-methylbutyl nitrite (Fig. 1b) show strong negative density gradients after about 2 μs that are captured by the simulations. The experimental signals for *neo*-pentyl nitrite (Fig. 1c) and *n*-pentyl nitrite (Fig. 1d) however mainly remain positive whereas the simulations turn slightly negative. At slightly higher temperatures (~880 K) the experimental profiles for *neo*-pentyl nitrite and *n*-pentyl nitrite resemble those in Figs. 1a and 1b. The data shown in Figs. 1c and 1d show the point at which the exothermic reactions are just becoming competitive with the endothermic reactions. This situation results in the experimental signal fluctuating close to the baseline value later in the experiment and the small difference between the simulation and experimental data under this condition is not of concern.

As previously noted, dissociation of all four nitrites is primarily initiated by O-NO bond cleavage to form an alkoxy radical which effectively eliminates formaldehyde instantaneously to give a butyl radical. From the simulation results at t_0 the rate coefficients for dissociation of the alkyl nitrite is obtained. Arrhenius plots for each of the nitrites are shown in Fig. 8. There are no apparent dependencies on either concentration or pressure, consistent with unimolecular reaction at or near the high pressure limit. The solid lines in Fig. 8 are from least squares fits to the experimental data with RMS deviations of 18 – 27%. An example of the sensitivity of the simulations to dissociation of the nitrites is shown in Fig. 9 for *iso*-butyl nitrite, reaction 1.1. Similar sensitivities were also found to reactions 2.1, 3.1 and 4.1. Literature rate constants were not available for dissociation of pentoxy isomers and values were taken by analogy with butoxy radicals, $>3\times10^9$ s^{-1} at 800 K, from Curran et al.[22] and errors due to this approximation are negligible due to the very large rate coefficients.

The remaining reactions in Tables 3 and 4 arise from reaction of the butyl radical isomers. These reactions are discussed for each isomer separately, but some general comments can be made regarding all the isomers. Dissociation of the resulting alkyl radical, R, typically proceeds through a primary channel at the temperatures studied here, producing smaller radicals (CH_3 and C_2H_5) or H-atoms. The simulations are insensitive to these reactions due to their small endothermicities ($\Delta H_{r,298K}$ = 11 – 22 kcal/mol). However, subsequent reactions of the radicals produced by the butyl radical isomers are mostly strongly exothermic and have a marked effect on the simulations. The

This journal is © The Royal Society of Chemistry 20xx

Please do not adjust margins

butyl radical isomers also undergo combination and H-abstraction (disproportionation) reactions, both of which are highly exothermic processes. Thus, within the secondary chemistry the butyl radical isomers can be consumed in a number of competitive exothermic reactions and the LS experiments alone are not sufficient to constrain the reaction mechanism.

The theoretical portion of this work plays an important part in developing constraints for the mechanisms, particularly with respect to radical recombination processes. Klippenstein et al.[27] have studied R + CH_3 and R + R reactions where R = CH_3, ethyl, *iso*-propyl and *tert*-butyl. The results of their calculations are shown in Fig. 2 along with results from this work for *sec*-butyl and *iso*-butyl. As is evident in Fig. 2, steric hindrance has a strong effect on the computed combination rate coefficients. For example, the rate coefficient for CH_3 + CH_3 is ~100x faster than that for *tert*-butyl + *tert*-butyl at temperatures relevant to the present study. The calculated rate coefficients for *sec*-butyl + *sec*-butyl are in line with these trends and they are up to a factor of two faster than the previously reported rate

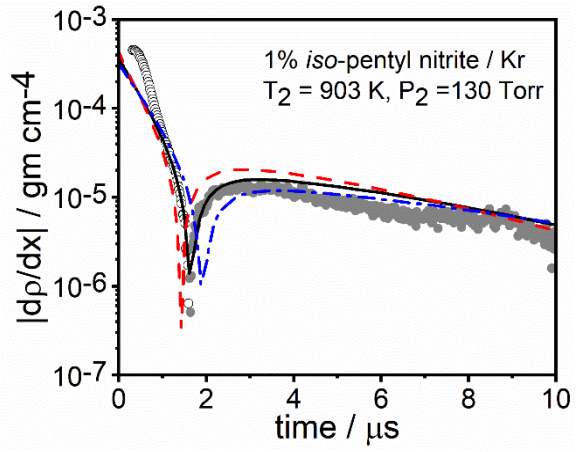

Figure 9: Sensitivity to 30% variation in k1.1, dissociation of *iso*-pentyl nitrite. Solid line – final model; Red, dash line – k1.1 +30%; Blue dash dot line – k1.1 – 30%.

coefficients for the more hindered *tert*-butyl reactions. Similar trends are observed for combination of the butyl radicals with methyl radicals (Fig. 2a). For example, the *iso*-butyl + CH_3 rate coefficients are ~33% greater than those for *sec*-butyl + CH_3 for T = 700 – 1200 K, as may be anticipated by their respective primary and secondary radical sites. The degree of steric hindrance influences not only the combination rate coefficients, but it also affects the ratio of disproportionation to recombination. Gibian and Corley reviewed the available data on the four butyl radicals and concluded that the disproportionation/recombination ratios increase depending on the number of abstractable H-atoms and the nature of the radical site, i.e. primary < secondary < tertiary.[24] It is interesting to note that these literature studies characterized the disproportionation/recombination ratios at room temperature with some limited studies[53] over extended temperature ranges. In the absence of detailed theoretical studies, these room-temperature ratios have been assumed valid for extrapolations to higher temperatures. The availability of accurate high-level theoretical predictions for atom-radical[37] and radical-radical[27] recombinations and high-level theoretical predictions for selected disproportionation reactions[56] allows us to make some limited observations on the temperature dependencies of disproportionation/recombination ratios. Specifically, in the case of radical-radical recombinations, Klippenstein et al.[27] predict that the capture rate constants drop by a factor of 3 - 7 over 300 - 1000 K with a steeper drop observed in the case of tertiary radicals relative to primary radicals. On the other hand, radical-radical disproportionations are predicted[56] to have a small positive temperature dependence and therefore for the butyl radical-radical reactions we anticipate larger disproportionation/recombination ratios (from room temperature estimates) at the higher temperatures relevant to the present work. The TOF-MS results for the *iso*-butyl radical that were discussed earlier support this conclusion and further experimental studies on other radical systems will be useful to support theoretical studies of disproportionation reactions.[24]

A final set of reactions from the theoretical work that are included in the reaction mechanisms are especially important at low pressures and/or high temperatures. These arise from the formation of adducts with excess energy that can either be stabilized by collisions with bath gas to give closed shell products or dissociate prior to stabilization to give radical products. Such well-skipping channels have been evaluated for reaction of each butyl isomer with their major β-scission decomposition product and are included in the final mechanisms.

***iso*-Pentyl nitrite and the *iso*-butyl radical:** Recombination and disproportionation of *iso*-butyl occur by reactions 1.4 and 1.5 respectively and the branching ratio of 0.3 from the TOF-MS experiments was used in the simulations. Little difference in the simulation results was observed when the branching ratio from Gibian and Corley[24] was substituted. This is because it results in only a relatively small change in flux through reaction 1.5 and which is compensated for by a corresponding increase in flux through alternate channels that have similar exothermicities. No literature data were available for either $k_{1.4}$ or $k_{1.5}$, therefore $k_{1.4}$ was calculated by VRC-TST. As expected, the recombination reaction is less favorable at higher temperatures; $k_{1.4}$ varies from 5.3×10^{12} to 2.8×10^{12} $cm^3mol^{-1}s^{-1}$ between 700 – 1000 K at 130 Torr. In Fig. 2b $k_{1.4}$ is compared with rate coefficients for other alkyl radical recombination reactions that were studied by Klippenstein et al.[27] At the temperatures of these experiments, the rate coefficient for *iso*-butyl + *iso*-butyl is approximately 5 times smaller than that for ethyl + ethyl, but similar in magnitude to *iso*-propyl + *iso*-propyl, and approximately 3 times larger than *tert*-butyl + *tert*-butyl.

Dissociation of *iso*-butyl occurs mainly by reaction 1.3 to give CH_3 and C_3H_6. There is also a minor dissociation channel to *iso*-butene + H with a rate coefficient approximately 0.04 × $k_{1.3}$.[22] As noted in the TOF-MS work, *iso*-butane and *iso*-butene were formed in equal amounts consistent with reaction 1.4 being minor. Initial estimates for $k_{1.3}$ were obtained from transition state theory calculations by Knyazev and Slagle for He and N_2

bath gases.[23] The best fit to the LS experiments was obtained by increasing the values of $k_{1.3}$ calculated for each pressure by a factor of 2.5, which is reasonable considering the differences in bath gases and the uncertainties in the calculated values.[23] Reaction 1.3 is quite fast, varying from 1.2×10^4 s^{-1} at 700 K to 2.2×10^6 s^{-1} at 1000 K and 130 Torr. Propene was a major product in the TOF-MS studies consistent with these rate coefficients. Consequently, methyl radicals are produced in abundance over the complete experimental range. However, methyl radicals were not observed in the mass spectra suggesting they were consumed rapidly. A sub-mechanism for CH_3 recombination based on prior DFTS/LS studies[57,58] is part of the complete mechanism. Simulation results indicate that methyl recombination is the major sink of methyl radicals and simulations indicate that ethane is a significant product. The IE of ethane is 11.5 eV, and therefore ethane would not be detected in the experiments with the MgF_2 filter. In the experiments without the filter, ethane was ionized but its mass is the same as NO and H_2CO. There is a step in the measured photoionization signal for m/z 30 without the MgF_2 filter that corresponds to the ionization energy of ethane but quantification of this signal is not feasible.

The theoretical work indicates that, at the LS experimental conditions, the reaction CH_3 + *iso*-butyl forms an energized complex that can be stabilized to give *iso*-pentane, reaction 1.6, or decompose by well-skipping channels to radical products, reactions 1.7 and 1.8. The competition between reactions 1.6 – 1.8 was evaluated by master equation calculations that were described earlier and the temperature dependencies for various pressures are shown in Fig. 7. The stabilization channel, reaction 1.6, is favored at high pressure and low temperature with reactions 1.7 and 1.8 becoming increasingly important at lower pressures and higher temperatures. For example, at 130 Torr the branching ratio, $k_{1.6}$ / ($k_{1.6}$+$k_{1.7}$+$k_{1.8}$), ranges from approximately 95% at 700 K to approximately 45% at 1000 K. The significant change in branching ratio over this temperature range indicates the key role addition-elimination channels play in product distributions, and demonstrates the potential importance of these types of reactions for simulating alkyl radical chemistry, particularly at high-temperatures (T > 1000 K). The sensitivity of the simulations to $k_{1.6}$ is demonstrated in Fig. 1a. The effect is relatively small as reduced flux through reaction 1.6 is compensated for by increased flux through other channels with similar enthalpies of reaction. However, factors of 2 change in $k_{1.6}$ do cause unacceptable changes in first two microseconds and the ability to locate the transition from net positive to net negative density gradient, an important target. As the pressure is increased to 10 bar, the range of the TOF-MS experiments, the branching ratio is nearly 100% at 700 K and approximately 90% at 1000 K indicating addition-elimination channels are insignificant at the conditions of the TOF-MS studies.

2-Methylbutyl nitrite and the sec-butyl radical: The dissociation of *sec*-butyl is similar to *iso*-butyl and it primarily produces CH_3 and C_3H_6 (reaction 2.3). There is also a minor channel that eliminates an H-atom that is even less significant than the corresponding path from *iso*-butyl. The path accounts for <1% *sec*-butyl and leads to 1-butene and 2-butene. Knyazev et al. studied this process in a combined experimental and theoretical study[25] and obtained pressure-dependent rate coefficients for He and N_2 bath gases. The expressions for He bath gas were adopted as a starting point for the kinetics model presented here but were increased by a factor of four to achieve the best fit to the experimental data.

sec-Butyl radicals recombine to produce 3,4-dimethylhexane (3,4-DMH). Similar to *iso*-butyl recombination (reaction 1.4), there was a lack of available literature data, and $k_{2.4}$ was calculated via VRC-TST and the results are shown in Fig. 2. The values of $k_{2.4}$ are intermediate between the rate coefficients for *iso*-propyl + *iso*-propyl and *tert*-butyl + *tert*-butyl calculated by Klippenstein et al.[27] As a secondary radical, the ratio of disproportionation to recombination is higher than for *iso*-butyl and other primary radicals due in part to steric hindrance. Based on values tabulated in the review by Gibian and Corley,[24] the ratio chosen here is 0.66, which is split evenly between formation of butane + 1-butene and butane + 2-butene (reactions 2.5 and 2.6, respectively). The combination reaction between *sec*-butyl and CH_3 (reaction 2.7) producing *iso*-pentane was also obtained from master equation calculations. The sensitivity of the density gradient to this reaction is shown in Fig. 1b. As with *iso*-butyl + CH_3, consideration was also given to the addition-elimination reaction to the lower-energy products, *i*-C_3H_7 and C_2H_5 (reaction 2.8) via well-skipping channels. Compared to *iso*-butyl + CH_3 the well-skipping channels are minor over the range of LS experiments and account for about 10% of the flux through *sec*-butyl + CH_3.

This journal is © The Royal Society of Chemistry 20xx

Please do not adjust margins

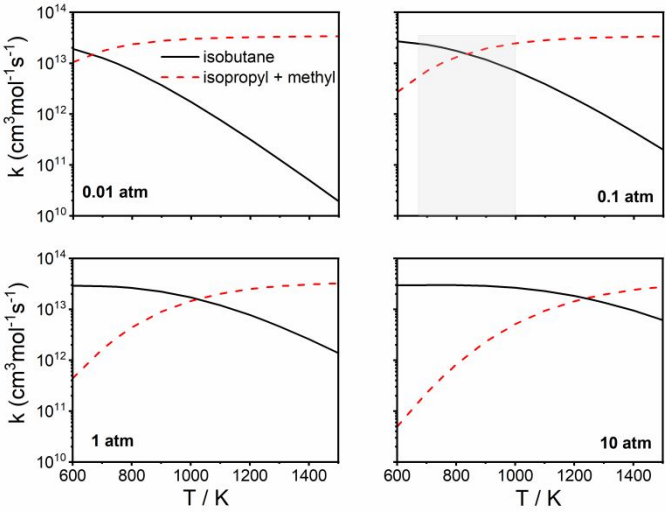

Figure10: Rate coefficients for combination and addition-elimination reactions for *tert*-butyl + H from master equation calculations at various pressures. The shaded grey rectangle shows approximate experimental conditions in this study.

***neo*-Pentyl nitrite and the *tert*-butyl radical:** In contrast to *iso*-butyl and sec-butyl, which dissociate to produce a methyl radical, the most favorable channel for *tert*-butyl dissociation is loss of an H-atom to produce *iso*-butene (3.3). Knyazev et al. also studied the dissociation of *tert*-butyl via a combined experimental and theoretical investigation.[26] Being a highly hindered tertiary radical, H-abstraction reactions occur faster than combination reactions. For example, for *tert*-butyl + *tert*-butyl, the disproportionation reaction is 3.1 times faster than the recombination to form 2,2,3,3-tetramethylbutane (2233-TMB).[24] The density gradient simulations are sensitive to $k_{3.5}$, Fig. 1c due to the relatively high rate of reaction and exothermicity ($\Delta H_{r,298\ K}$ = -62.8 kcal/mol). Reaction between *tert*-butyl radicals and hydrogen atoms can proceed by addition (reaction 3.6), addition-elimination (reaction 3.8) or direct abstraction (reaction 3.7). The rate coefficients for reactions 3.6 and 3.8 were obtained from master equation calculations and the temperature dependencies for selected pressures are shown in Fig. 10. The temperature and pressure dependencies are similar to those for *iso*-butyl nitrite + CH_3. The branching ratio $k_{3.6}$ / ($k_{3.6}$+$k_{3.8}$) at 135 Torr ranges from 96% at 700 K to 59% at 1000 K. At a pressure of 10 atm, the branching fraction is nearly 100% at 700 K and approximately 97% at 1000 K. The direct abstraction channel, reaction 3.7, forming *iso*-butene + H_2 is expected to be faster than addition, reaction 3.6, in the sterically hindered *tert*-butyl radical and we estimated $k_{3.7} = 2 \times k_{3.6}$.

***n*-Pentyl nitrite and the *n*-butyl radical:** *n*-Butyl dissociation forms an ethyl radical and ethylene with a minor channel (0.2%) producing H + butene. This reaction was studied by Knyazev and Slagle, by a transition state model based on available literature data,[23] and later by Zheng and Blowers using G3 and complete basis set composite energy methods.[28] The rate coefficients used in the current modelling work are approximately a factor of 2 lower than the Knyazev and Slagle

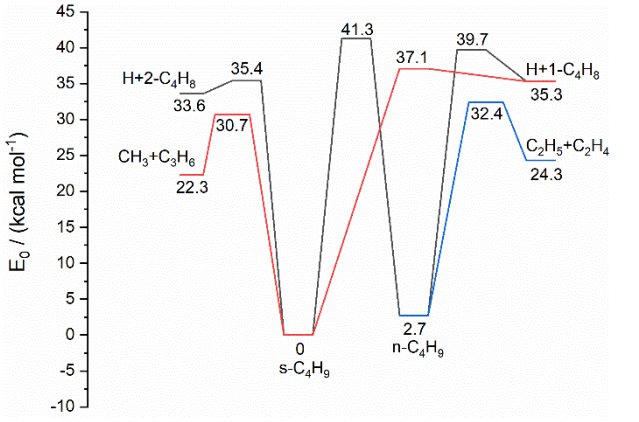

Figure 11: Principle pathways for the isomerization and dissociation of *n*-butyl and *sec*-butyl radicals at the CCSD(T)/cc-pvinfz//M062x/cc-pvtz level of theory.

numbers, and within 30-40% of the Zheng and Blowers numbers. At the conditions of the current work, dissociation of ethyl radical is negligible except at the highest temperatures.[2] Potentially, *n*-butyl can isomerize to *sec*-butyl.[52] However, the isomerization involves a four-center hydrogen migration that has a barrier of 38.6 kcal/mol at the CCSD(T)/cc-pvinfz//M062x/cc-pvtz level of theory. In contrast to this, beta-scission of *n*-butyl to C_2H_5+C_2H_4 has a barrier 29.7 kcal/mol, Fig. 11. Consequently, isomerization is expected to be a negligible channel relative to the facile beta-scission process.[59] *n*-Butyl radicals undergo recombination to produce *n*-octane (4.4). Rate coefficients for this reaction were calculated by VRC-TST similar to the analogous reactions for *iso*-butyl and *sec*-butyl radicals. The rate coefficient is slightly lower (25-30%) than the ethyl + ethyl recombination rate coefficient calculated by Klippenstein et al.[27] As a primary radical, disproportionation producing butane and butene (4.5) is a relatively minor channel, and has a rate coefficient equal to 14% that for recombination.[24]

The ethyl radical produced from dissociation of *n*-butyl can add to *n*-butyl producing hexane (4.6). Rate coefficients for reaction 4.6 were calculated for the experimental temperatures and pressures of the LS work. Reaction 4.6 competes with two disproportionation channels reactions 4.7 and 4.8. In reaction 4.7 the ethyl radical abstracts an H-atom from *n*-butyl while in reaction 4.8 *n*-butyl abstracts an H-atom from ethyl. The branching ratios for these reactions relative to reaction 4.6 was obtained from Gibian and Corley,[24] as ($k_{4.6}$ / $k_{4.7}$) = 0.08 and ($k_{4.6}$ / $k_{4.8}$) = 0.06. The simulations are quite sensitive to $k_{4.6}$ as shown in Fig. 1d.

The laser schlieren and theoretical studies probed a broad range of reaction conditions and different types of reactions dominated in various regimes. A short summary of the key features follows. At the lower-temperature range (<900 K), self-reactions of the four butyl radicals were the dominant reactions, and unsurprisingly, molecular structure predicated the recombination to disproportionation ratios in these radicals. The present experiments support the associated theoretical studies on the self-recombination kinetics of the four butyl radicals. However, the kinetics of the

Please do not adjust margins

disproportionation processes relied on literature estimates of the branching ratios. Theoretical studies of these disproportionation reactions that involve a barrierless abstraction process require challenging multi-reference electronic structure theory calculations.[56] These are being characterized in a separate theoretical study.

At T > 900 K, the butyl radicals dissociate and initiate secondary reactions. In particular, simulations of the present experiments are influenced by bimolecular reactions of the four butyl radicals with their corresponding dominant β-scission radical products (H, CH_3, and C_2H_5). Theoretical studies of these processes indicate that these reactions not only proceed through the recombination (and disproportionation/abstraction) processes discussed earlier but that these reactions form chemically activated C_4 - C_6 alkanes that can dissociate to other radical products. Fig. 12 summarizes the results from the present theoretical studies and plots the probabilities for radical recombination over the 0.01-100 atm pressure range at 1000 K. The role of energy transfer, pressure, molecular structure, and molecular size is reflected in these results with well-skipping to CH_3 + *iso*-C_3H_7 being the dominant process in the *tert*-butyl + H reaction at P < 1 atm. On the other hand, recombination to form *n*-hexane is the dominant process even at 0.01 atm in the C_2H_5 + *n*-butyl molecular system. Theoretical calculations indicate that well-skipping processes are important at T > 1000 K for even the larger C_2H_5 + *n*-butyl molecular system studied here and suggest the inclusion of such processes for characterizing the high-temperature kinetics of alkyl radicals and alkanes. In summary, the present experimental results and associated kinetic modelling of these aided by theory present a more detailed picture of alkyl radical reaction kinetics at high temperatures over a range of pressures relevant to practical processes.

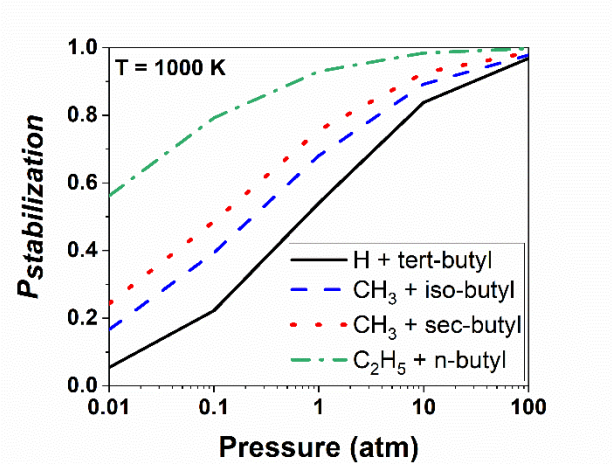

Figure 12: Probability for stabilization to C4-C6 alkanes from corresponding radical reactants of interest. Solid line – *iso*-C4H10, dashed and dotted lines – *iso*-C5H12, dashed-dotted line – *n*-C6H14.

Conclusions

A unified picture of the chemistry of four butyl radical isomers has been developed in the auto-ignition region where competition between oxidation and pyrolysis reactions is important. Studying the four radicals with the same experimental and theoretical method has allowed the rich chemistry in this region to be developed. The butyl isomers contain primary, secondary, and tertiary radical sites and varying degrees of steric hindrance. These factors were found to influence the decomposition and addition reactions of the radicals in a manner consistent with expectations from the limited literature. High pressure limit rate coefficients for dissociation for the four nitrites were obtained. To the best of our knowledge there are no prior data on these, and they will facilitate the use of the nitrites as radical sources in other studies. The TOF-MS studies provided a unique insight into the decomposition mechanism of *iso*-pentyl nitrite. In particular, the results confirmed that NO loss is the dominant path and as far as we are aware provided the first experimental evidence for thermal elimination of HNO from an alkyl nitrite and estimate of the branching fraction between the dominant NO loss channel and HNO elimination. The mechanism by which HNO is eliminated is unknown and may be via a roaming channel. Further experimental study to examine the effects of molecular structure on the production of HNO coupled with theoretical investigations may address this issue and facilitate the use of nitrites as radical sources. The product distributions observed in the TOF-MS data at high pressures are consistent with the reaction mechanism proposed for *iso*-pentyl nitrite at low pressures from the LS studies. Both the TOF-MS and LS studies support the conclusions of the theoretical study of *iso*-butyl + CH_3 and the pressure and temperature dependent competition between stabilization and well-skipping reactions. Additionally, the TOF-MS data was used along with prior literature studies to obtain rate constants for the disproportionation reaction of *iso*-butyl radicals. A schematic summarizing the mechanism is given in Fig. 6 and is easily extended to the other isomers. For each of the nitrites a complete reaction mechanism is provided that includes pressure dependent expressions to facilitate their use at conditions other than studied here. There is very limited information with regards to the C4 alkyl radical self reactions and its reactions with H, CH_3, and C_2H_5 radicals in detailed kinetics models. These reactions are not included even in recent state-of-the-art detailed kinetics models such as ARAMCO MECH 3.0[60] that were specifically developed for C4 alkanes. These recent models do include the alkyl radical dissociation processes which are described with pressure-dependence.

Conflicts of interest

There are no conflicts of interest to declare.

Acknowledgements

This material is based on work supported by the U.S. Department of Energy, Office of Basic Energy Sciences, Division

This journal is © The Royal Society of Chemistry 20xx

Please do not adjust margins

of Chemical Sciences, Geosciences, and Biosciences through Argonne National Laboratory. Argonne is a U.S. Department of Energy laboratory managed by UChicago Argonne, LLC, under contract DE-AC02-06CH11357. The LS work was conducted in the Chemical Dynamics in the Gas Phase Program. The ANL-HRRST experiments were conducted in the Argonne/Sandia Consortium on High Pressure Combustion Chemistry.

This research used resources of the Advanced Light Source, which is a DOE Office of Science User Facility under contract no. DE-AC02-05CH11231. The experiments were performed at beamline 9.0.2.

References

1 R. S. Tranter, A. W. Jasper, J. B. Randazzo, J. P. A. Lockhart and J. P. Porterfield, *Proc. Combust. Inst.*, 2017, **36**, 211–218.

2 J. B. Randazzo, M. E. Fuller, C. F. Goldsmith and R. S. Tranter, *Proc. Combust. Inst.*, 2019, **37**, 703–710.

3 J. A. Miller, S. J. Klippenstein, S. H. Robertson, M. J. Pilling, R. Shannon, J. Zádor, A. W. Jasper, C. F. Goldsmith and M. P. Burke, *J. Phys. Chem. A*, 2016, **120**, 306–312.

4 J. D. DeSain, S. J. Klippenstein and C. A. Taatjes, *Phys. Chem. Chem. Phys.*, 2003, **5**, 1584–1592.

5 E. G. Estupiñán, S. J. Klippenstein and C. A. Taatjes, *J. Phys. Chem. B*, 2005, **109**, 8374–8387.

6 N. J. Labbe, R. Sivaramakrishnan and S. J. Klippenstein, *Proc. Combust. Inst.*, 2015, **35**, 447–455.

7 R. S. Tranter and B. R. Giri, *Rev. Sci. Instrum.*, 2008, **79**, 094103.

8 J. B. Randazzo and R. S. Tranter, *Rev. Sci. Instrum.*, 2015, **86**, 016117.

9 J. H. Kiefer, Z. Al-Alami and J.-C. Hajduk, *Appl. Opt.*, 1981, **20**, 221–230.

10 J. H. Kiefer, in *Shock Waves in Chemistry*, ed. A. Lifshitz, Marcel Dekker, New York, 1981.

11 W. C. Gardiner, Y. Hidaka and T. Tanzawa, *Combust. Flame*, 1981, **40**, 213–219.

12 Chemspider, http://www.chemspider.com/Chemical-Structure.9632, (accessed 24 March 2019).

13 Chemspider, http://www.chemspider.com/Chemical-Structure.2308, (accessed 24 March 2019).

14 Chemspider, http://www.chemspider.com/Chemical-Structure.456989, (accessed 24 March 2019).

15 W. C. Gardiner, B. F. Walker and C. B. Wakefield, in *Shock Waves in Chemistry*, ed. A. Lifshitz, Marcel Dekker, New York, 1981.

16 E. Goos, A. Burcat and B. Ruscic, Extended Third Millenium Ideal Gas Thermochemical Database with updates from Active Thermochemical Tables.

17 C. W. Gao, J. W. Allen, W. H. Green and R. H. West, *Comput. Phys. Commun.*, 2016, **203**, 213–225.

18 Reaction Mechanism Generator, https://rmg.mit.edu/molecule_search, (accessed 1 June 2017).

19 B. Ruscic and D. H. Bross, Active Thermochemical Tables (ATcT) values based on ver. 1.122 of the Thermochemical Network, https://atct.anl.gov/, (accessed 20 August 2017).

20 R. S. Tranter and P. T. Lynch, *Rev. Sci. Instrum.*, 2013, **84**, 094102.

21 P. T. Lynch, T. P. Troy, M. Ahmed and R. S. Tranter, *Anal. Chem.*, 2015, **87**, 2345–2352.

22 H. J. Curran, *Int. J. Chem. Kinet.*, 2006, **38**, 250–275.

23 V. D. Knyazev and I. R. Slagle, *J. Phys. Chem.*, 1996, **100**, 5318–5328.

24 M. J. Gibian and R. C. Corley, *Chem. Rev.*, 1973, **73**, 441–464.

25 V. D. Knyazev, I. A. Dubinsky, I. R. Slagle and D. Gutman, *J. Phys. Chem.*, 1994, **98**, 11099–11108.

26 V. D. Knyazev, I. A. Dubinsky, I. R. Slagle and D. Gutman, *J. Phys. Chem.*, 1994, **98**, 5279–5289.

27 S. J. Klippenstein, Y. Georgievskii and L. B. Harding, *Phys. Chem. Chem. Phys.*, 2006, **8**, 1133–1147.

28 X. Zheng and P. Blowers, *Theor. Chem. Acc.*, 2007, **117**, 207–212.

29 T. A. Cool, A. McIlroy, F. Qi, P. R. Westmoreland, L. Poisson, D. S. Peterka and M. Ahmed, *Rev. Sci. Instrum.*, 2005, **76**, 094102.

30 D. L. Osborn, P. Zou, H. Johnsen, C. C. Hayden, C. A. Taatjes, V. D. Knyazev, W. North, D. S. Peterka, M. Ahmed, S. R. Leone, D. L. Osborn, P. Zou, H. Johnsen, C. C. Hayden, C. A. Taatjes, V. D. Knyazev, S. W. North, D. S. Peterka, M. Ahmed and S. R. Leone, *Rev. Sci. Instrum.*, 2008, **79**, 104103.

31 Chemspider, http://www.chemspider.com/Chemical-Structure.7762, (accessed 24 March 2019).

32 S. J. Klippenstein, *J. Chem. Phys.*, 1991, **94**, 6469–6482.

33 S. J. Klippenstein, *J. Chem. Phys.*, 1992, **96**, 367–371.

34 J. M. L. Martin, *Chem. Phys. Lett.*, 1996, **259**, 669–678.

35 J. A. Miller and S. J. Klippenstein, *J. Phys. Chem. A*, 2003, **107**, 2680–2692.

36 S. J. Klippenstein, A. F. Wagner, R. C. Dunbar, D. M. Wardlaw, S. H. Robertson and J. A. Miller, Variflex, version 2.02m. (unpublished) Argonne National Laboratory (2010).

37 L. B. Harding, Y. Georgievskii and S. J. Klippenstein, *J. Phys. Chem. A*, 2005, **109**, 4646–4656.

38 B. E. Poling, J. M. Prausnitz and J. P. O'Connell, *The Properties of Gases and Liquids*, McGraw-Hill, New York, 2001.

39 A. W. Jasper, C. M. Oana and J. A. Miller, *Proc. Combust. Inst.*, 2015, **35**, 197–204.

40 K. P. Kim and J. V. Michael, *Symp. Combust.*, 1994, **25**, 713–719.

41 S. J. Klippenstein, L. B. Harding and Y. Georgievskii, *Proc. Combust. Inst.*, 2007, **31**, 221–229.

42 P. T. Lynch, *Rev. Sci. Instrum.*, 2016, **87**, 056110.

43 P. J. Linstrom and G. W. Mallard, Eds., *NIST Chemistry WebBook, NIST Standard Reference Database Number 69*, National Institutes of Standards and technology, Gaithersburg, MD, 20899.

44 K. Watanabe, *J. Chem. Phys.*, 1957, **26**, 542–547.

45 P. Erman, A. Karawajczyk, E. Rachlew-Källne and C.

Strömholm, *J. Chem. Phys.*, 1995, **102**, 3064–3076.

46 Y. Ono, S. H. Linn, H. F. Prest, C. Y. Ng and E. Miescher, *J. Chem. Phys.*, 1980, **73**, 4855–4861.

47 P. C. Killgoar, G. E. Leroi, J. Berkowitz and W. A. Chupka, *J. Chem. Phys.*, 1973, **58**, 803–806.

48 O. Welz, J. Zador, J. D. Savee, M. Y. Ng, G. Meloni, R. X. Fernandes, L. Sheps, B. A. Simmons, T. S. Lee, D. L. Osborn and C. A. Taatjes, *Phys. Chem. Chem. Phys.*, 2012, **14**, 3112–3127.

49 B. Yang, J. Wang, T. A. Cool, N. Hansen, S. Skeen and D. L. Osborn, *Int. J. Mass Spectrom.*, 2012, **309**, 118–128.

50 J. Wang, B. Yang, T. A. Cool, N. Hansen and T. Kasper, 2008, **269**, 210–220.

51 B. Rotavera, *Private communication*, .

52 B. Rotavera, J. Za, O. Welz, L. Sheps, A. M. Scheer, J. D. Savee, M. A. Ali, T. S. Lee, B. A. Simmons, D. L. Osborn, A. Violi and C. A. Taatjes, *J. Phys. Chem. A*, 2014, **118**, 10188–10200.

53 D. H. Slater, S. S. Collier and J. G. Calvert, *J. Am. Chem. Soc.*, 1968, **90**, 268–273.

54 J. O. Terry and J. H. Futrell, *Can. J. Chem.*, 1968, **46**, 664–665.

55 T. A. Cool, K. Nakajima, T. A. Mostefaoui, F. Qi, A. Mcllroy, P. R. Westmoreland, M. E. Law, L. Poisson, D. S. Peterka and M. Ahmed, *J. Chem. Phys.*, 2003, **119**, 8356–8365.

56 C. H. Wu, D. B. Magers, L. B. Harding, S. J. Klippenstein and W. D. Allen, *J. Chem. Theory Comput.*, 2020, **16**, 1511–1525.

57 X. Yang, C. Franklin Goldsmith and R. S. Tranter, *J. Phys. Chem. A*, 2009, **113**, 8307–8317.

58 X. Yang, A. W. Jasper, J. H. Kiefer and R. S. Tranter, *J. Phys. Chem. A*, 2009, **113**, 8318–8326.

59 J. A. Miller and S. J. Klippenstein, *J. Phys. Chem. A*, 2013, **177**, 2718–2727.

60 C. Zhou, Y. Li, U. Burke, C. Banyon, K. P. Somers, S. Ding, S. Khan, J. W. Hargis, T. Sikes, O. Mathieu, E. L. Petersen, M. Alabbad, A. Farooq, Y. Pan, Y. Zhang, Z. Huang, J. Lopez, Z. Loparo, S. S. Vasu and H. J. Curran, *Combust. Flame*, 2018, **197**, 423–438.

This journal is © The Royal Society of Chemistry 20xx

Please do not adjust margins

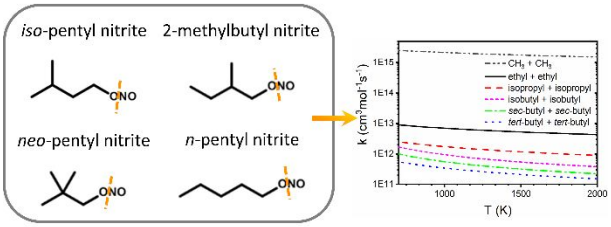

Insights into the structure dependence of butyl radicals in recombination, disproportionation and nonthermal reactions in the autoignition region.